Iio et al. Earth, Planets and Space (2017) 69:144
DOI 10.1186/s40623-017-0730-3

Earth, Planets and Space

FULL PAPER Open Access

Which is heterogeneous, stress or strength? An estimation from high-density seismic observations

Yoshihisa Iio[1*], Itaru Yoneda[1], Masayo Sawada[1], Tsutomu Miura[1], Hiroshi Katao[1], Yoichiro Takada[2], Kentaro Omura[3] and Shigeki Horiuchi[4]

Abstract

Using data from high-density seismic observation networks installed in the western Nagano Prefecture region in Japan, we precisely determined focal mechanisms and estimated the high-resolution stress field at a scale of 1 km. Almost all differences between observed and calculated slip directions (misfit) were smaller than the errors in focal mechanisms at grid points away from the mainshock fault. This finding clearly indicates that the estimated uniform stress suitably explains focal mechanisms in each subregion apart from the mainshock fault. Misfits are relatively large at grid points near the mainshock fault, but many of these misfits are smaller than the errors in focal mechanisms, and stress is regarded as uniform for a greater portion within each subregion. However, we found that focal mechanisms and *P*-axes varied widely and differed from each other for a short focal distance of 100 m. These results clearly show that stress can be regarded as uniform, but that strength is heterogeneous.

Keywords: Stress, Heterogeneity, Fault strength, Stress inversion, Focal mechanism

Introduction

It has long been believed that stress in the Earth's crust is highly heterogeneous. Borehole measurements show orientations of maximum horizontal compressive stress varying by tens of degrees in the upper several kilometers (e.g., Barton and Zoback 1994; Wilde and Stock 1997). Heterogeneous slip distributions along faults are attributed to heterogeneity in the stress acting on those faults, as well as in fault strength (e.g., Andrews 1980; Ben-Zion and Sammis 2003). Furthermore, heterogeneous focal mechanisms have been observed in aftershock areas close to faults associated with large earthquakes, which suggests local stress heterogeneity (e.g., Michael et al. 1990; Hauksson 1994).

However, these observations do not necessarily indicate that stress in the crust is typically heterogeneous, particularly in seismogenic regions. Borehole measurements reflect the stress state only in the shallow crust, where earthquakes rarely occur. Heterogeneous slip distributions and focal mechanisms are often observed in limited portions on or near earthquake faults. Furthermore, because heterogeneous slip distributions are generally estimated assuming smooth, planar faults, heterogeneous stress and strength are necessary to explain observations, whereas complex fault geometries, such as offset or bend of faults, generally are not considered. In addition, variations of focal mechanisms may be explained not only by heterogeneous stress but also by heterogeneous strength of faults (e.g., Rivera and Kanamori 2002).

To clarify whether stress in the crust is heterogeneous, it is important to precisely estimate that stress at fine scales. Presently, stress inversion of focal mechanisms is the most reliable method by which stress can be estimated in seismogenic regions. The orientations of three principal stresses and the ratio of their differences, which can be estimated as the difference between an observed slip direction and calculated one, are minimized in an analysis area, as schematically shown in Fig. 1a (e.g.,

*Correspondence: iio@rcep.dpri.kyoto-u.ac.jp
[1] Research Center for Earthquake Prediction, Disaster Prevention Research Institute, Kyoto University, Uji, Japan
Full list of author information is available at the end of the article

Gephart and Forsyth 1984; Michael 1984, 1987). It is assumed that stress is uniform throughout the analysis area and that faults slip along the direction of maximum shear stress.

However, there is a fundamental question under debate about what the results of stress inversion reflect. Smith and Heaton (2011) proposed that they reflect not the orientations of the three principal stresses but those of incremental stresses, as shown in Fig. 1b. Because it is assumed in stress inversion that stress is uniform throughout an analysis area, fault strength is inferred to vary depending on the orientations of faults (Rivera and Kanamori 2002). However, Smith and Heaton (2011) proposed that each fault is subjected to individual stress to which that fault is most favorably oriented. In other words, if an earthquake occurs on a fault, a fault plane with a different orientation is subjected to a different stress that produces maximum shear along the slip direction. In this case, it is inferred that the orientations of *P*-axes of focal mechanisms are in accordance with those of the maximum compressional stress, particularly if the fault strength is small. Furthermore, each fault is assumed to exist under a critical stress state in which the magnitude of shear stress on the fault is comparable to its strength. In this case, if incremental stress is added, only a fault with stress that is favorable to the incremental stress can break.

Recently, changes in stress before and after large earthquakes have been observed for several aftershock areas (Hardebeck and Hauksson 2001; Yoshida et al. 2014, 2015). The findings suggest that the magnitudes of differential stresses are much smaller than expected from results of frictional experiments in laboratories (Byerlee 1978), which Smith and Heaton (2011) regard as artifacts, as they reflect stress changes (incremental stress) generated by earthquake slips. However, Hardebeck (2010) reported results that contradict the view of Smith and Heaton (2011). They estimated stress fields before and after large earthquakes based on stress inversion of focal mechanisms and showed that the focal mechanisms of aftershocks are mainly controlled by the stress before large earthquakes. Furthermore, Hardebeck (2015) argued that the assumption of errors in focal mechanisms in the simulation by Smith and Heaton (2011) was inadequate.

If the hypothesis of Smith and Heaton (2011) holds and focal mechanisms of earthquakes that occur close to each other are significantly different, stress must change over small distances. However, such change is not easy to occur because stress should satisfy the condition of continuity. Actually, Smith and Heaton (2011) assumed a spatial correlation in stress distribution at the kilometer scale. Therefore, to resolve this problem, it is important to clarify how stress changes in space. In this study, we precisely determined focal mechanisms and estimated spatial changes in stress using high-quality data from a dense seismic observation network installed in the western Nagano prefecture region, Japan.

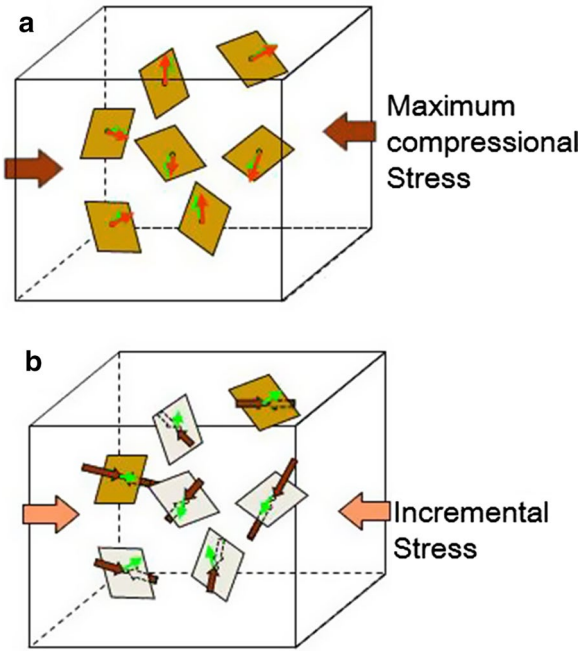

Fig. 1 Two different explanations of focal mechanisms. **a** A case of ordinary stress inversions (e.g., Gephart and Forsyth 1984; Michael 1984, 1987). Stress is assumed to be uniform in the analysis area. Small rectangles indicate faults. Green and red arrows indicate observed slip directions from focal mechanisms and calculated slip directions inferred from the direction of maximum shear on the fault, respectively. Brown arrows indicate axes of the maximum compressional stress. **b** Hypothesis of Smith and Heaton (2011). Each fault plane is subjected to different maximum compressional stress, as indicated by brown arrows. Earthquake slips occur only on the faults indicated by colored rectangles, on which the stress has a similar orientation to the incremental stress

Data

Geophysical setting of western Nagano prefecture region

We have analyzed data from high-density seismic observation networks installed in the western Nagano prefecture region. The 1984 Western Nagano Prefecture Earthquake (Mj 6.8) occurred in this region on September 14, 1984, about 10 km southeast of Mt. Ontake, which erupted in 2015. The earthquake fault was estimated by Yoshida and Koketsu (1990) to be right lateral and ENE–WSW trending, as shown in Fig. 2. Seismic activity has remained high for over 30 years after the mainshock. This

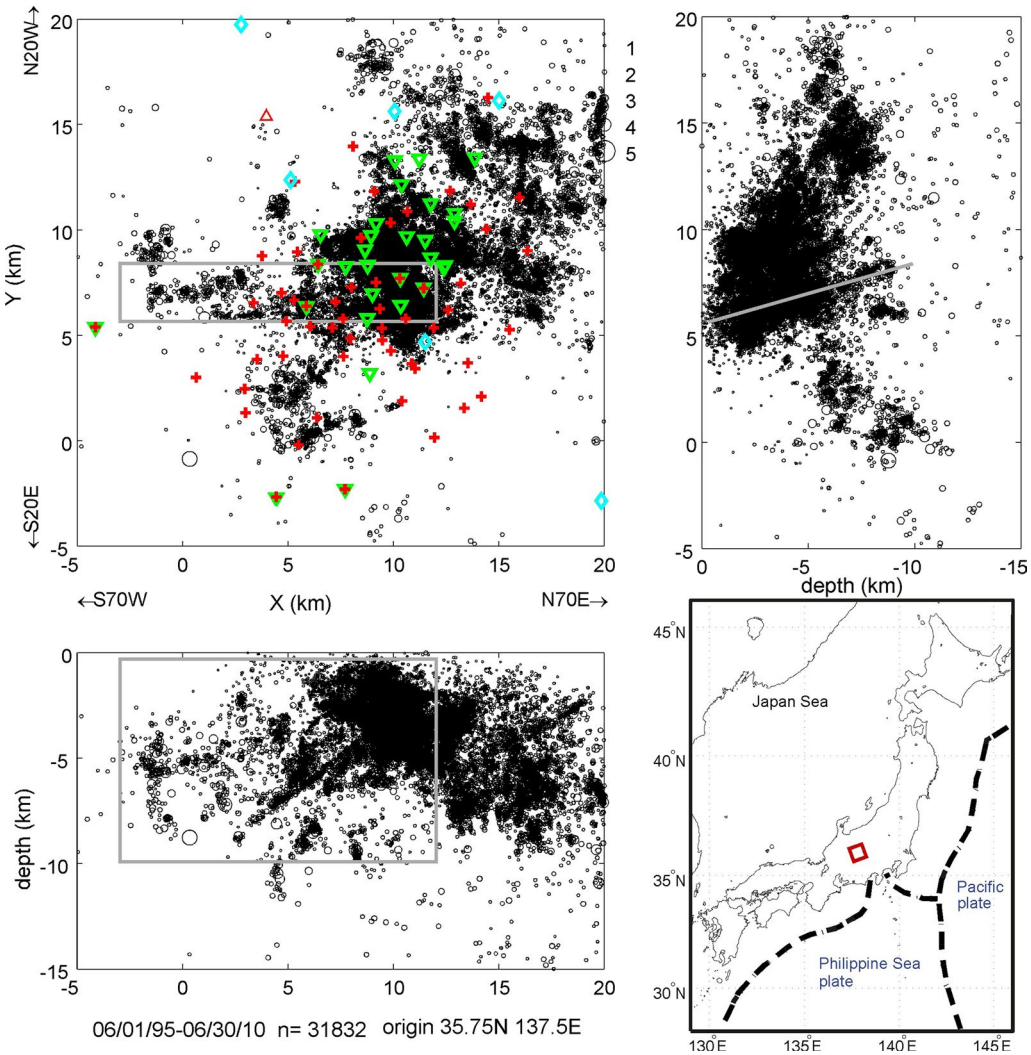

Fig. 2 Locations of hypocenters of events analyzed in this paper, the earthquake fault (blue rectangle) estimated by Yoshida and Koketsu (1990), and seismic stations. Locations of seismic stations of the high-sampling and Manten observation networks and permanent stations (operated by NIED, JMA, and Nagoya University) are indicated by red crosses, green reversed triangles, and cyan diamonds, respectively. Black circles are earthquakes used in this study, which occurred from June 1995 to June 2010. Red rectangle in the large-scale map indicates the study area

seismic activity is not only distributed along the mainshock fault plane but also includes swarm-like activity in the eastern part of the source region (Fig. 2). Most of the hypocenters are concentrated within shallow layers at depths of 1–8 km.

Dense seismic observations

For this paper, we have used the data from two different semi-stationary seismic observation networks. The first is the high-sampling observation network, which has operated from 1995 to the present (Iio et al. 1999). This observation network consists of 57 stations (at maximum) spaced at 1–4 km apart, as indicated by red crosses in Fig. 2. These stations are installed on bedrock in a mountainous region to minimize background seismic noise. Waveforms are recorded at a 10 kHz sampling rate with 16-bit resolution on high- and low-gain channels, only when the recording system is triggered. Examples of waveforms in the vertical component are shown in Fig. 3; onsets of *P*-waves are clear and their pulses are isolated, which suggest that the estimated arrival times of both *P*- and *S*-waves are accurate. The clocks are corrected by GPS every 2 h such that uncertainties in the absolute time are less than 1 ms. These high-quality data have enabled various detailed analyses of the initial rupture processes of microearthquakes (Iio et al. 1999; Iio

2009), source parameters of small earthquakes (Imanishi et al. 2004; Matsuzawa et al. 2004; Venkataraman et al. 2006), precise hypocentral distributions (Rydelek et al. 2002; Cheng et al. 2007), 3D velocity structure at the kilometer scale (Doi et al. 2013), and stress state (Yukutake et al. 2010).

The second network, the Manten seismic observation network, has operated from August 2008 to the present with 29 stations equipped with the Manten system, which is a newly developed seismic observation instrument composed of a small, light, and portable velocity-type sensor (2 Hz) and an extremely low-power data logger (Iio 2011). Waveforms are recorded continuously at a 250 Hz sampling rate with 18-bit resolution. The clocks are corrected by GPS every 1 h such that uncertainties in the absolute time are less than 1 ms. These stations are installed mainly in the central part of the area with swarm activity, as indicated by green inverted triangles in Fig. 2. At stations marked by both a red cross and a green inverted triangle, the Manten system was installed after removal of the high-frequency observation system. Permanent stations (cyan diamonds) operated by the National Institute for Earth Science and Disaster Prevention (NIED), the Japan Meteorological Agency (JMA) and Nagoya University were also used. These continuous recordings enabled us to determine focal mechanisms of very small earthquakes down to magnitudes of zero.

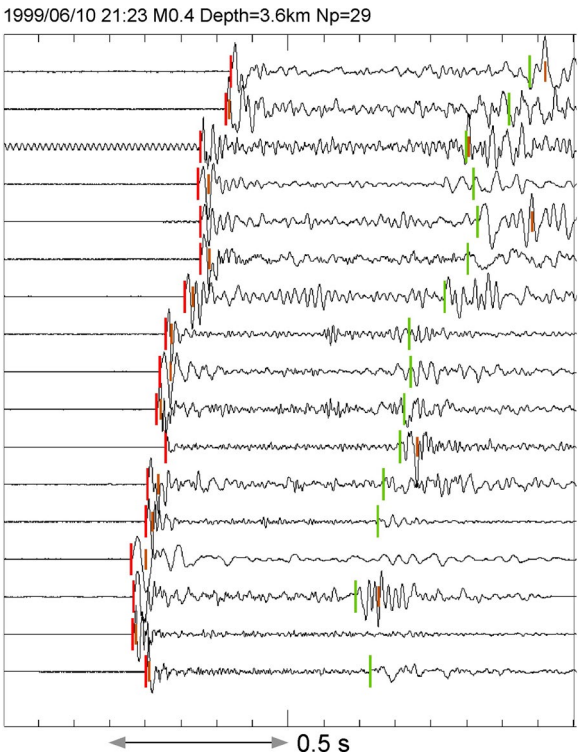

Fig. 3 Examples of waveforms in the vertical component recorded by the high-frequency observation network. Waveforms are displayed in order of epicentral distances. Red and green bars indicate visually picked arrival times of *P*- and *S*-waves, respectively. Brown bars indicate locations of maximum amplitude. The arrival times of *S*-waves were picked on transverse components, not shown in this figure

Results

Focal mechanisms

We used the data collected from June 1995 to June 2010. For before August 2008, only data from the high-sampling observation network were used, whereas data from both networks were used for August 2008 and later. We determined focal mechanisms as follows. *P*- and *S*-wave arrival times were picked visually, as shown in Fig. 3. Transverse components were used for *S*-wave picking to reduce the effects of converted waves such as Sp phases. The picking errors of *P*- and *S*-wave arrival times for the high-sampling data were estimated as 2 and 30 ms, respectively (Doi et al. 2013), which indicates very high accuracy, whereas the picking errors of *P*-wave arrival times for the Manten observation were slightly larger because of the lower sampling rate of 250 Hz. Hypocenters were determined using the modified Hypomh program (Hirata and Matsu'ura 1987) in which *S*-wave velocity structure can be set independently of *P*-wave structure (Kawanishi et al. 2009). We employed a one-dimensional velocity structure with 10 layers of widths of 0.1–2 km estimated using the joint hypocenter determination (JHD) method (Asaka et al. 2005). First, we calculated station corrections as averages of O–C for *P*- and *S*-wave arrival times at each station, using only large events for which the number of *P*-wave arrivals was greater than 20. Standard deviations of the station corrections were 25 and 46 ms for *P*- and *S*-wave arrival times, respectively. After these corrections, the RMSs of O-C of P- and S-arrival times for each event were less than 10 ms and a few tens of ms, respectively. Thus, we could determine relative hypocenters very accurately, and many relative errors were estimated as several tens of m and about 100 m in the horizontal and vertical directions, respectively.

Focal mechanisms were determined using the program of Maeda (1992), in which all the fault plane solutions with the least inconsistent polarities are extracted by a grid search with a spacing of about 8° in azimuth and dip directions of *B*-axis on the focal sphere. The best fault plane solution is then selected from these numeral solutions as follows. In the case of no inconsistent polarity, the fault plane solution is drawn apart from locations of

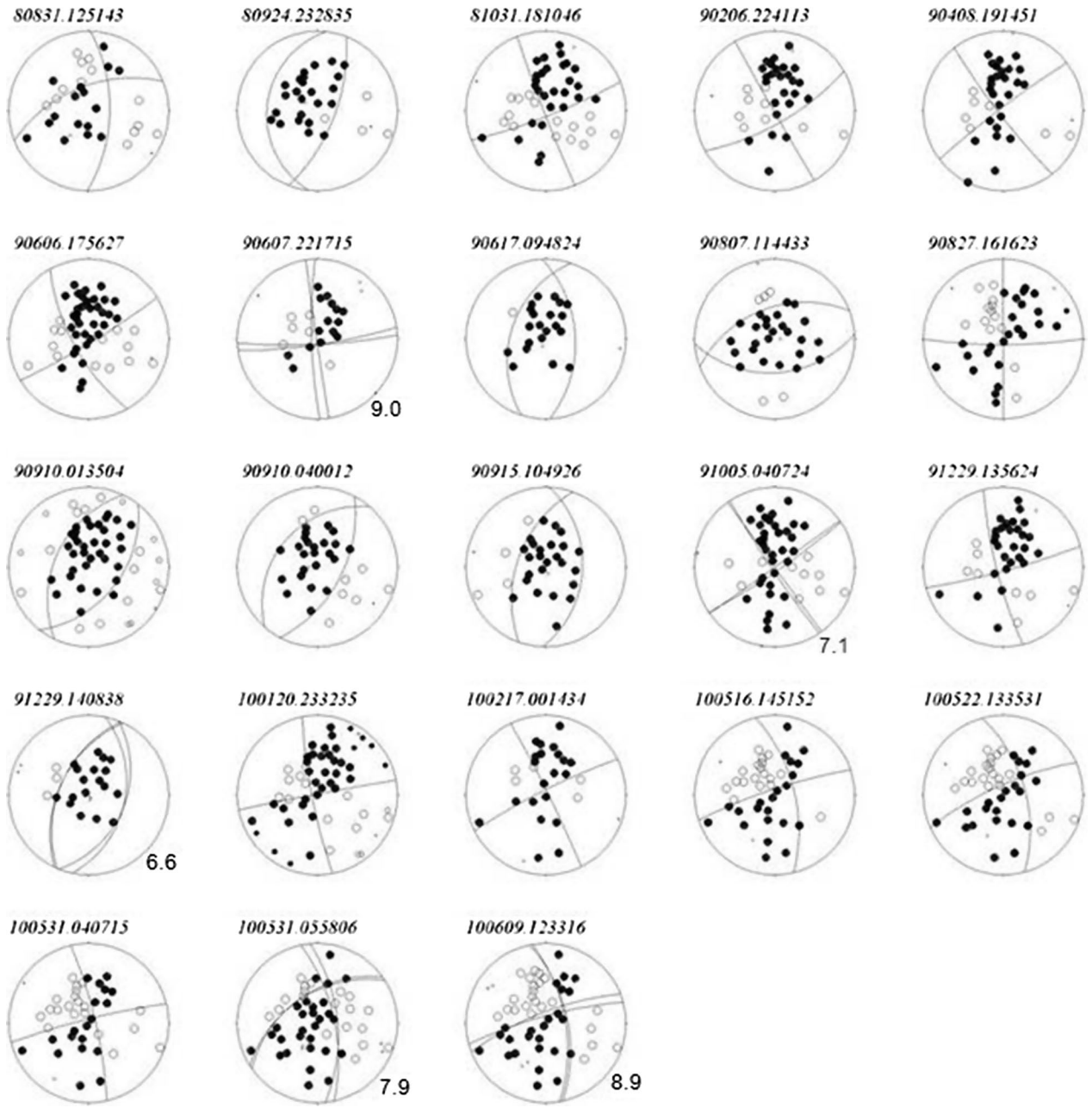

Fig. 4 Examples of estimated focal mechanisms in the upper hemisphere of the events in a subregion with dimensions of 1 km per grid point ($x = 9, y = 6, z = -3$). Focal mechanisms were determined using the program of Maeda (1992), in which all fault plane solutions with the least inconsistent polarities were extracted by a grid search with a spacing of about 8° in azimuth and dip directions of the *B*-axis on the focal sphere. Numerals shown to the lower right side of the focal mechanisms with plural solutions represent errors in focal mechanisms estimated from the largest differences between multiple numeric solutions

consistent stations projected on the focal sphere, whereas in other cases, it is drawn as close to the locations of inconsistent stations as possible.

Examples of estimated focal mechanisms are shown in Fig. 4. We used only focal mechanisms with 15 or more polarities. Furthermore, we estimated errors in focal mechanisms from the largest difference between plural solutions, measured according to the Kagan angle (the minimum rotation angle) (Kagan 1991), as shown in the lower right sides of focal mechanisms with plural solutions. Errors were estimated to be zero for focal mechanisms with only one solution. In this study, we used only the mechanisms with errors less than 10°. Consequently, we used 3041 well-constrained focal mechanisms from 31,832 earthquakes. The effects of three-dimensional velocity structure were not considered in this study, because focal distances are very small, and because lay paths are then thought to be less influenced by the estimated velocity perturbations (Doi et al. 2013).

Stress inversion

We estimated the stress field in the area shown in Fig. 2 using a standard stress inversion method in which the difference between the observed and calculated slip directions (misfit) is minimized, assuming uniform stress in an individual analysis area (e.g., Gephart and Forsyth 1984; Michael 1987). In this method, the root mean square of misfits is minimized. The fault plane is distinguished

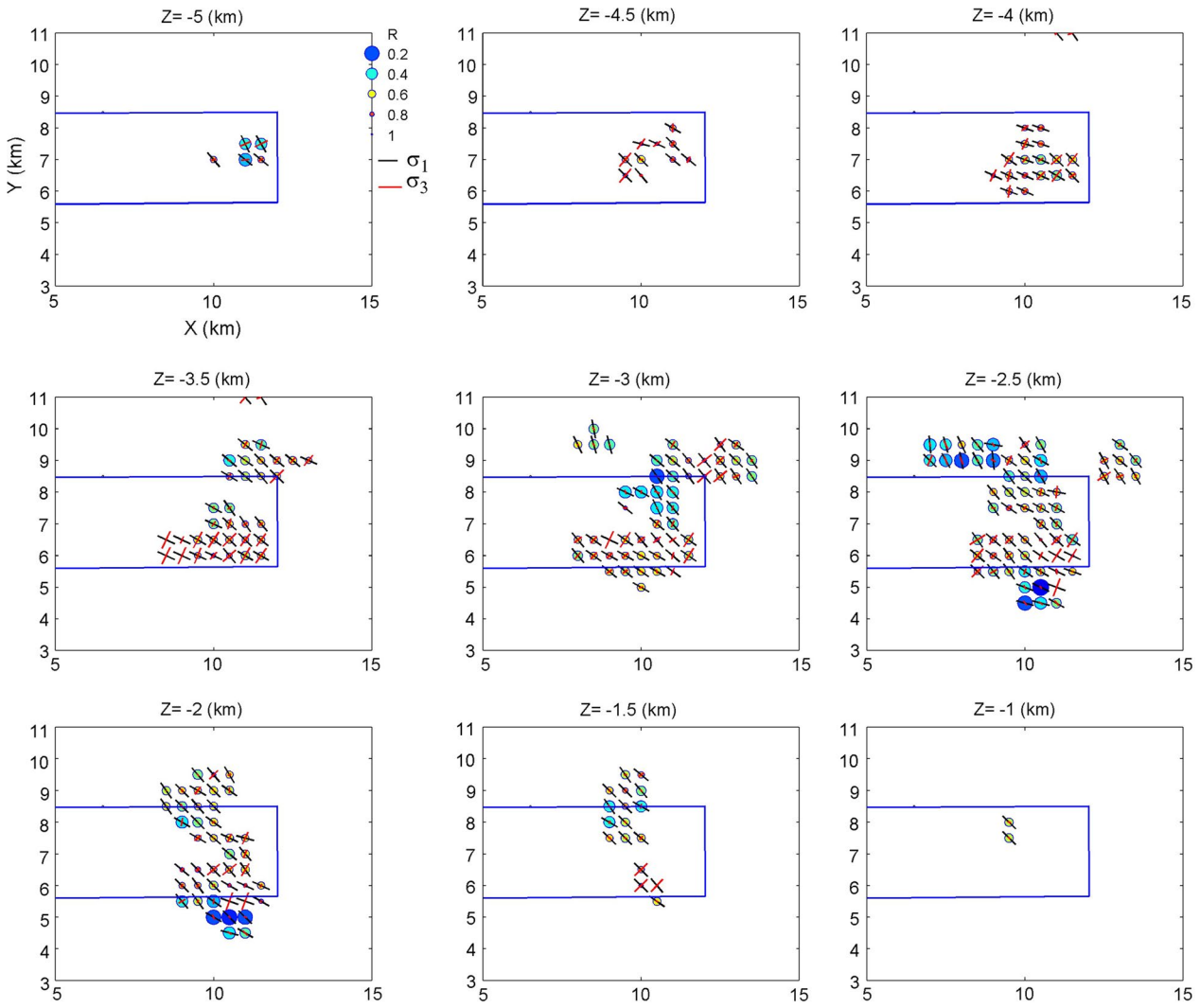

Fig. 5 Results of stress inversion projected onto horizontal planes. The maximum (σ_1) and minimum (σ_3) compressional stress axes are shown by black and red lines, respectively. The stress ratio *R* is shown by the dimensions and colors of filled circles. Blue rectangle is the earthquake fault estimated by Yoshida and Koketsu (1990). The coordinates are the same as those in Fig. 2

from the auxiliary plane based on the difference in misfits calculated for both the planes. When multiple focal mechanisms are determined, the focal mechanism with the least misfit is selected.

In the same study region, Yukutake et al. (2010) conducted a stress inversion analysis using high-sampling data from 1999 to 2011. They estimated stress at points on a three-dimensional grid with 1 km spacing using the focal mechanisms for which hypocenters were located in a cubic subregion with dimensions of 2 km. In this study, we estimated stress precisely in a subregion with dimensions of 1 km at grid points with 500-m spacing. We first performed a grid search for directions of the principal stress axes with 10° grid intervals and the stress ratio, $R\ (= (\sigma_1 - \sigma_2)/(\sigma_1 - \sigma_3))$, with 0.1 grid intervals. We repeated the grid search to seek better estimates of the directions of the principal stress axes with 5° grid intervals and the stress ratio with 0.05 grid intervals in the vicinity of the values estimated using the first grid search. Ninety-five percent confidence limits are calculated by a boot strap resampling method, repeating the above procedure 2000 times, following Michael (1987).

The results are shown in Figs. 5 and 6. Figure 5 shows that the maximum (σ_1) and minimum (σ_3) compressional stress axes projected on horizontal planes with a spacing of 500 m. Stress ratio R is also shown by filled circles. The 95% confidence limits of the maximum and minimum compressional stress axes projected onto horizontal planes are shown in Fig. 7. The directions of σ_1 are generally oriented from about 30° to 45° from the azimuth of the earthquake fault. Figure 6 shows σ_1 and σ_3 axes projected on vertical planes perpendicular to the fault strike of the mainshock. Many of the directions of the minimum compressional axes are nearly vertical at grid points away from the earthquake fault, whereas the directions of these axes are more varied near the earthquake fault,

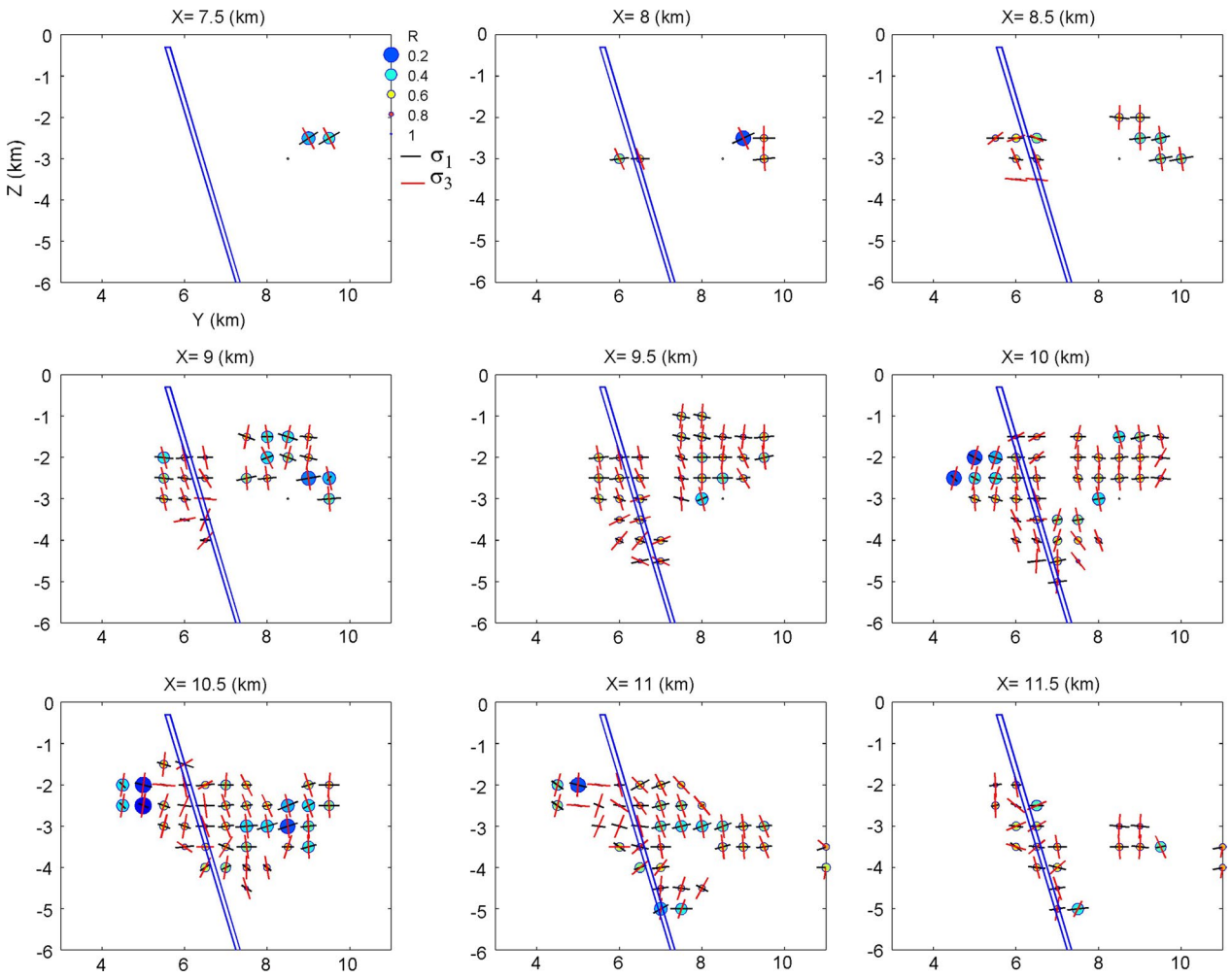

Fig. 6 Results of stress inversion projected onto vertical planes perpendicular to the fault strike of the mainshock. Other explanations are the same as for Fig. 5

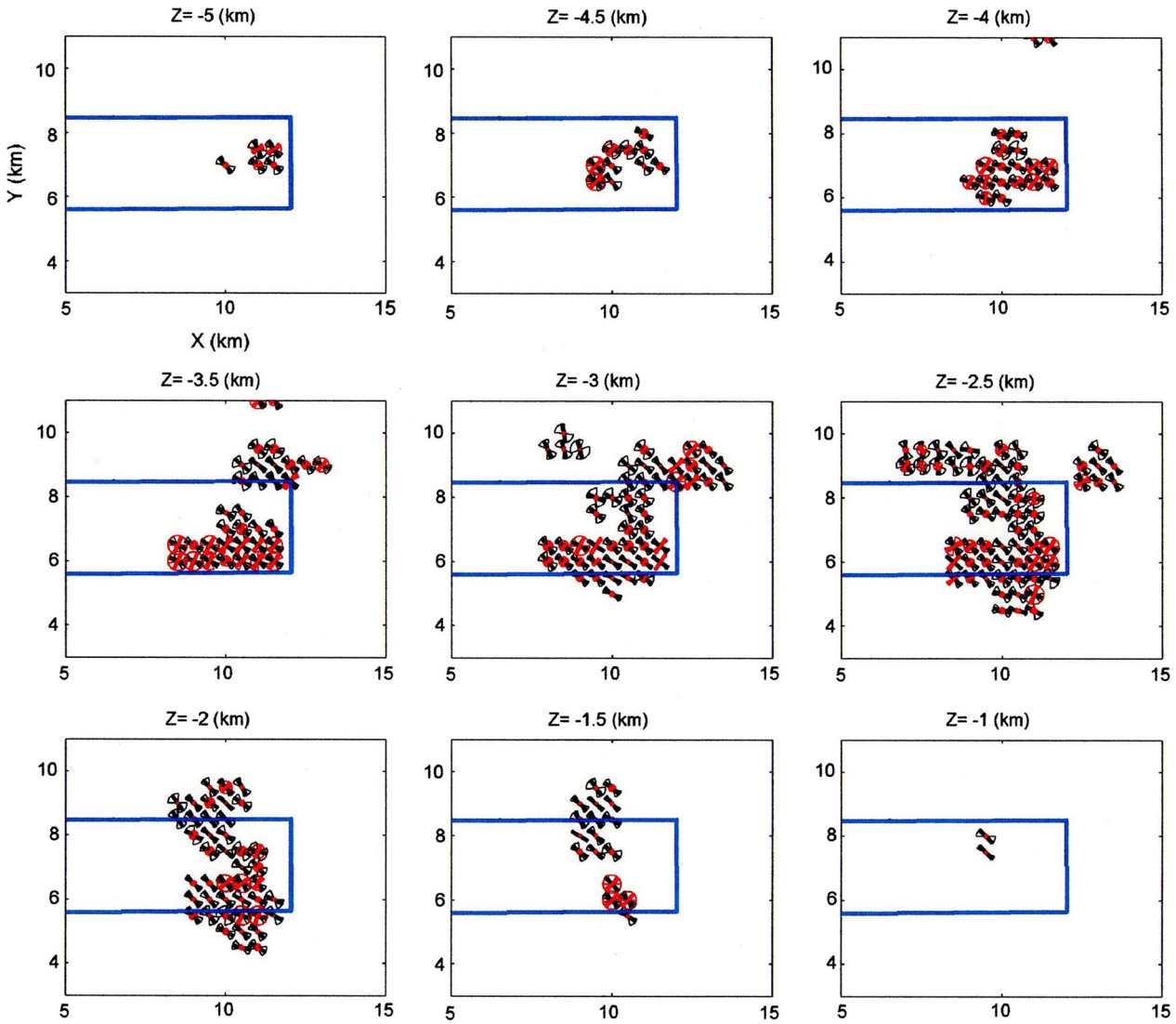

Fig. 7 95% confidence limits of the σ_1 and σ_3 axes are indicated by black and red fans, respectively. Other explanations are the same as for Fig. 5

including some that are horizontal, which indicates a strike-slip type of stress state.

Spatial changes in the σ_2 dip angles in the direction perpendicular to the fault strike are shown in Fig. 8a. It is seen that nearly vertical σ_2 axes are concentrated around the mainshock fault. A similar result was reported by Yukutake et al. (2010), and we confirmed their results in this study. Furthermore, stress ratios seemed to be larger around the mainshock fault than at grid points farther away from it. These results can be explained by aseismic slip in the downward extension of the mainshock fault, as pointed out by Yukutake et al. (2010). Figure 8b shows spatial changes in RMSs of differences between the observed and calculated slip directions (misfits) in the direction perpendicular to the fault strike. The root mean squares of misfits were small at grid points farther from the mainshock fault. This clearly indicates that the estimated uniform stress well explains the focal mechanisms at each grid point away from the mainshock fault. Namely, the stress field away from the mainshock fault can be regarded as uniform within a length scale of 1 km. However, across the entire analysis area, Figs. 5, 6, and 7 show that the stress field gradually change in space over a length scale longer than 1 km, mainly depending on the distance from the mainshock fault. Near the mainshock fault, it appears that RMS misfits are larger than

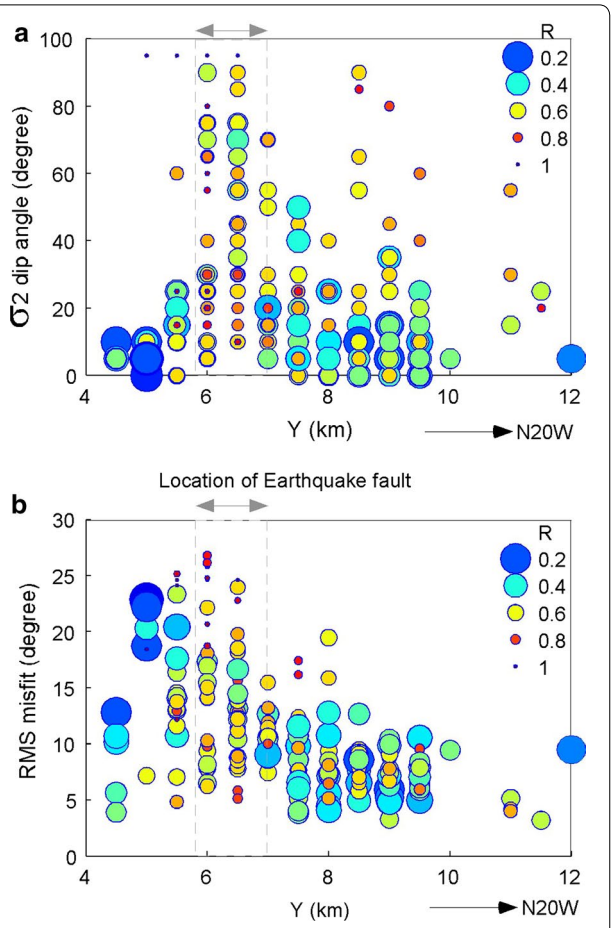

Fig. 8 Spatial changes in σ_2 dip angles (**a**) and root mean square (RMS) differences between observed and calculated slip directions (misfit) (**b**) in the direction perpendicular to the fault strike. Stress ratio *R* is indicated by the dimensions and colors of filled circles

the errors in focal mechanisms at more than half of grid points, which suggests that stress may be heterogeneous at those grid points.

Next, we have fully examined how the focal mechanism data are explained by the estimated stress. Figure 9 shows a typical example for a grid point ($x = 10$, $y = 9$, $z = -2$) away from the mainshock fault. The number of focal mechanisms at this grid point is 60, which is the maximum for grid points away from the mainshock fault. The 95% confidence limits were estimated using a bootstrap resampling method: 100° to 120°, − 5° to 15°, and − 15° to 30°, for azimuth and dip angle of σ_1 and dip angle of σ_2, respectively. Figure 9 demonstrates how observed slip directions are fitted by calculated slip directions. Rectangles are the estimated fault plane on which misfit is smaller than that on the other nodal plane. The observed and calculated slip directions almost overlap. Thus, it is found that focal mechanisms are well explained by the estimated uniform stress for this subregion.

We further examined the data fitting and the estimated stress state at this grid point. Figure 10a shows the normalized shear and normal stresses on a three-dimensional Mohr diagram. Pore pressure indicators, P_p, are calculated as $P_p = \sigma_n - \tau/\mu$, where μ is assumed as 0.6, the cohesion along the fault plane is ignored. P_p, σ_n, and τ are normalized by $\sigma_1 - \sigma_3$, because we determine not the magnitudes of absolute stresses but a stress ratio, $(\sigma_1 - \sigma_2)/(\sigma_1 - \sigma_3)$ by stress inversion. Furthermore, we set the base of the stress difference to σ_3, although this value can be set arbitrarily.

Figure 10a shows that the plots are scattered; however, half of the data with large P_p (i.e., larger than zero) have large differences of misfits between the fault plane and auxiliary plane (which we define as the 'misfitdiff'), which suggests that the selection of the fault plane is reliable for these data. Furthermore, Fig. 10b shows that a large proportion of the misfits are smaller than the error in focal mechanisms. Figure 10c shows that orientations of fault planes are distributed very widely, and any special focal mechanisms do not have large misfits. These plots suggest that stress in the subregion was well determined and can be regarded as uniform there. As shown in Fig. 10d, misfits did not show clear dependence on magnitude. Figure 10e shows that P_p values reach a peak around − 0.4, but more than half of them are widely distributed. Thus, the results likely do not reflect a special stress state in a small portion of this subregion.

The results shown in Figs. 9 and 10 were estimated for a single grid point; however, similar results were estimated for many grid points away from the earthquake fault. As shown in Fig. 8b, RMS misfits were small, and the orientations of fault planes are varied widely in these regions.

However, in regions near the earthquake faults, RMS misfits were relatively large, as shown in Fig. 8b. This finding is likely due to stress concentration by the mainshock slip along the earthquake fault. As an example of the results at grid points near the earthquake fault, we show fitting of the data and the estimated stress for a single grid point ($x = 9$, $y = 6$, $z = -3$) in Figs. 11 and 12. The number of focal mechanisms at this grid point was 89, the maximum across all grid points. The mainshock fault was located near $Y = 6.1$–6.3 in this depth range. Near the mainshock fault, many almost vertical fault planes with green or blue upper edges seem to be aligned in the direction of the *X*-axis, which is the azimuth of the mainshock fault, although their orientations varied widely. As shown in Fig. 11, even in this region, many observed slip directions were explained well by the estimated stress, although there was a tendency for misfits to be large near the mainshock fault. As shown in Fig. 12b, more than half of the misfits were smaller than the error in focal mechanisms. However, Fig. 12d displays a large

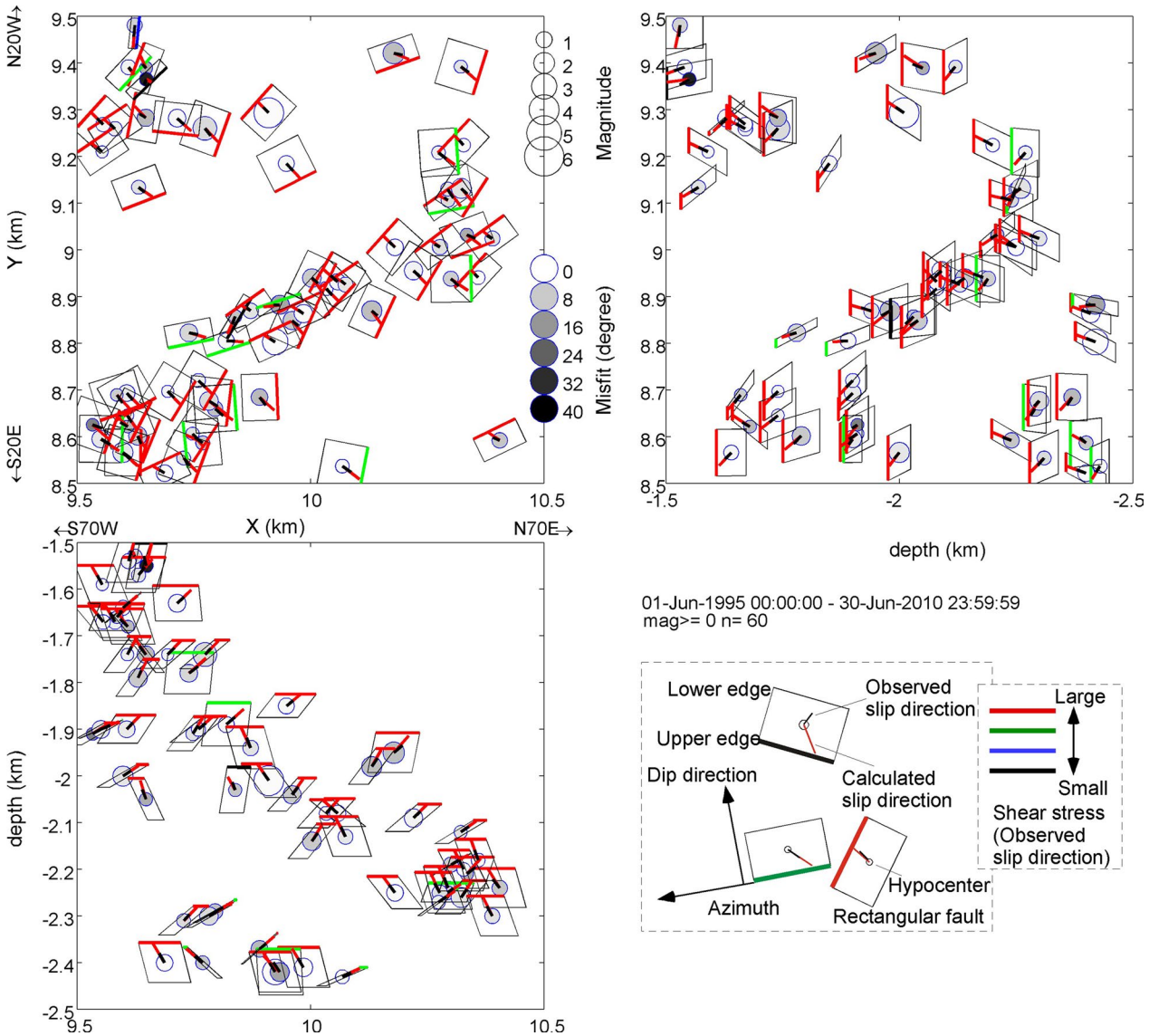

Fig. 9 Results of stress inversion for a grid point ($x = 10$, $y = 9$, $z = -2$) away from the mainshock fault. Rectangles are estimated fault planes projected onto the horizontal and two vertical sections. The upper edges of fault planes are indicated by thick colored edges, which represent the normalized shear stress on the fault plane based on color. Black, blue, green, and red indicate normalized shear stress of 0–0.2, 0.2–0.3, 0.3–0.4, and 0.4–0.5, respectively. Observed and calculated slip directions are shown by black (short) and red (long) bars at the center of the rectangle, respectively. Diameters and colors of circles represent magnitudes and misfits (difference between observed and calculated slip directions), respectively

misfit of about 100° and a few tens of misfits from 10° to 50°. The 95% confidence limits were estimated using a bootstrap resampling method, as 95° to 130°, − 20° to 15°, and − 85° to 85°, for azimuth, dip angle of σ_1, and dip angle of σ_2, respectively. The orientation of σ_1 was determined well, although the dip angle of σ_2 was not well constrained. Therefore, even in this region, those observed focal mechanisms were basically explained by the uniform stress, except for a smaller portion of the data with large misfits. Figure 12e shows that P_p values were widely distributed, which suggests that the strength of the fault strength may vary.

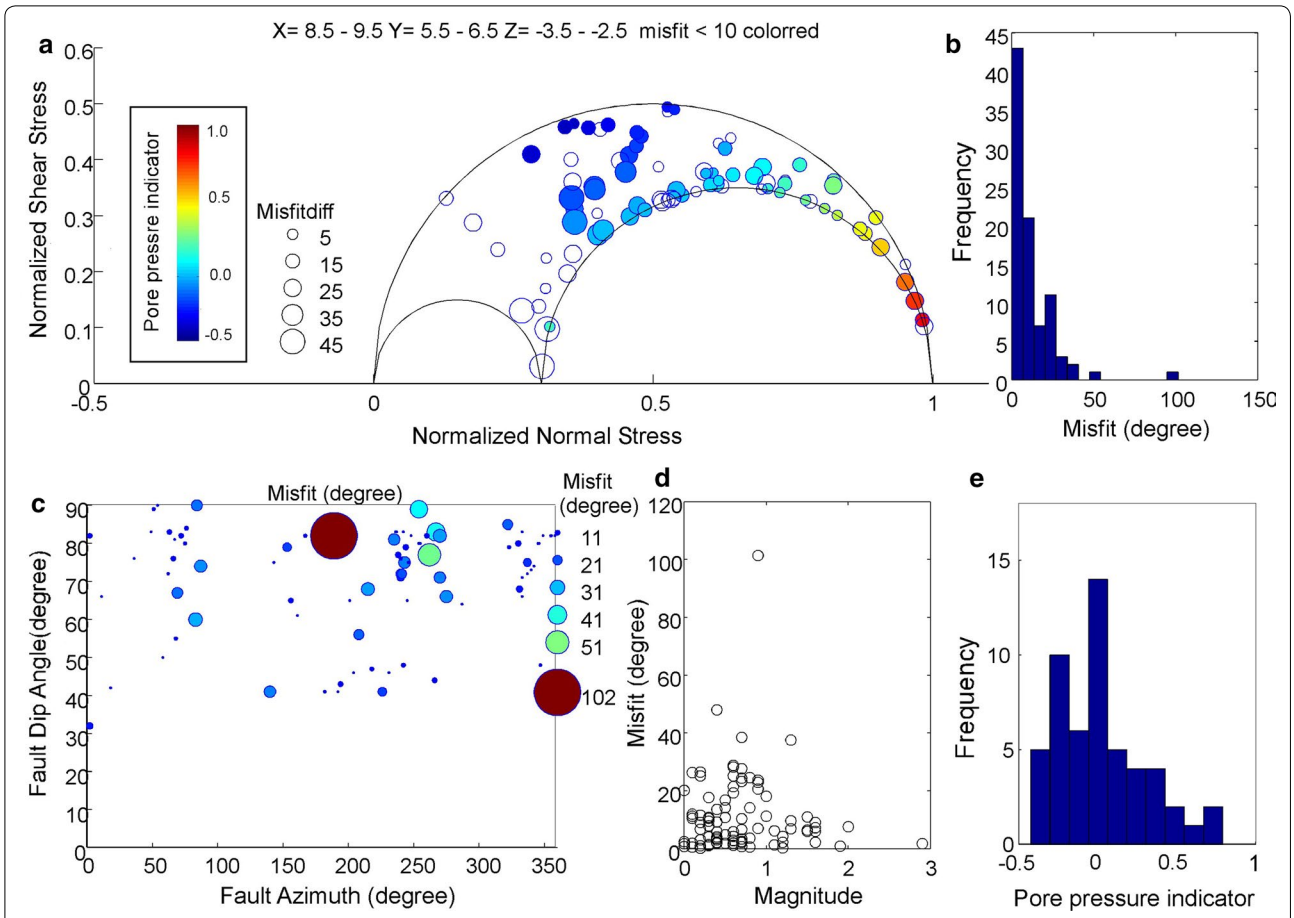

Fig. 10 **a** Plots of the normalized shear and normal stresses on faults on a three-dimensional Mohr diagram for a grid point ($x = 10, y = 9, z = -2$). Pore pressure indicators P_p are calculated as $P_p = \sigma_n - \tau/\mu$, where μ is assumed as 0.6. Sizes of circles represent the difference of misfits between the fault plane and auxiliary plane (misfitdiff); coloring indicates only data with misfits on the fault plane greater than the error of focal mechanisms, 10°. **b** Histogram of misfits. **c** Relationship between azimuths and dip angles of the fault planes. Misfits are also indicated by the sizes and colors of circles. **d** Relationship between magnitude and misfit. **e** Histogram of the pore pressure indicator, P_p. The following figure is that for Fig. 12

It is estimated from these analyses that the stress field can be regarded as uniform at a length scale of 1 km away from the mainshock fault, whereas it appears to be disordered in a smaller portion of the area, even in the subregions with dimensions of 1 km near the mainshock fault.

Discussion

Variety of focal mechanisms

It was found that focal mechanisms vary widely and that the observed data are well explained by uniform stress in a cubic subregion with dimensions of 1 km, except for a portion of the data for grid points near the earthquake faults. These results indicate that stress can be regarded as uniform over a small region at the kilometer scale, which suggests that the strength of faults varies greatly. Such uniformity of stress supports the validity of stress inversion analysis; however, it is thought to conflict with the hypothesis of Smith and Heaton (2011), which assumes heterogeneous stress. If their hypothesis holds, each fault is basically subjected to the stress to which it is most favorably oriented, and the orientations of the *P*-axes of focal mechanisms are thought to be in accordance with those of the maximum compressional stress axes. In particular, fault strength is small.

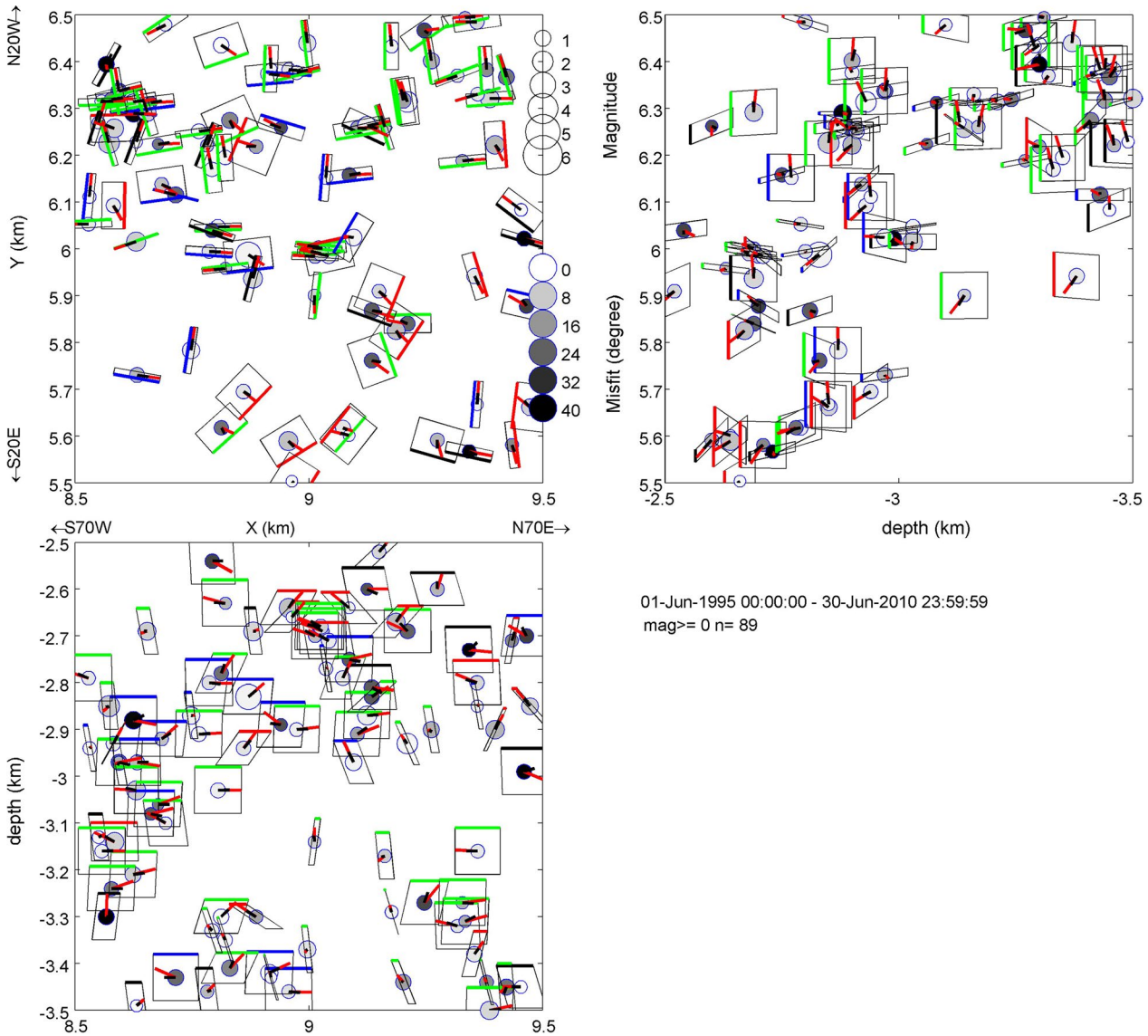

Fig. 11 Results of stress inversion for a grid point ($x = 9, y = 6, z = -2$) near the mainshock fault. Other explanations are the same as for Fig. 9

To clarify this inconsistency with the hypothesis of Smith and Heaton (2011), we investigated the differences in focal mechanisms between event pairs within a cubic subregion. Here, we only used the best fault plane solution if plural focal mechanisms were obtained. Figure 13 shows that the relationship between focal distances and the difference in *P*-axis orientations (the angle between *P*-axes) for each event pair for a single grid point ($x = 10, y = 9, z = -2$), and the frequency distribution of the angles between two *P*-axes for each event pair (in the upper panel). The angles between two *P*-axes varied widely, even for very short focal distances. Furthermore, it appears that the distribution of these angles does not significantly change with focal distance. The line indicates a moving average over 100 m, and this line is almost flat except for at long distances. In the lower panel, similar

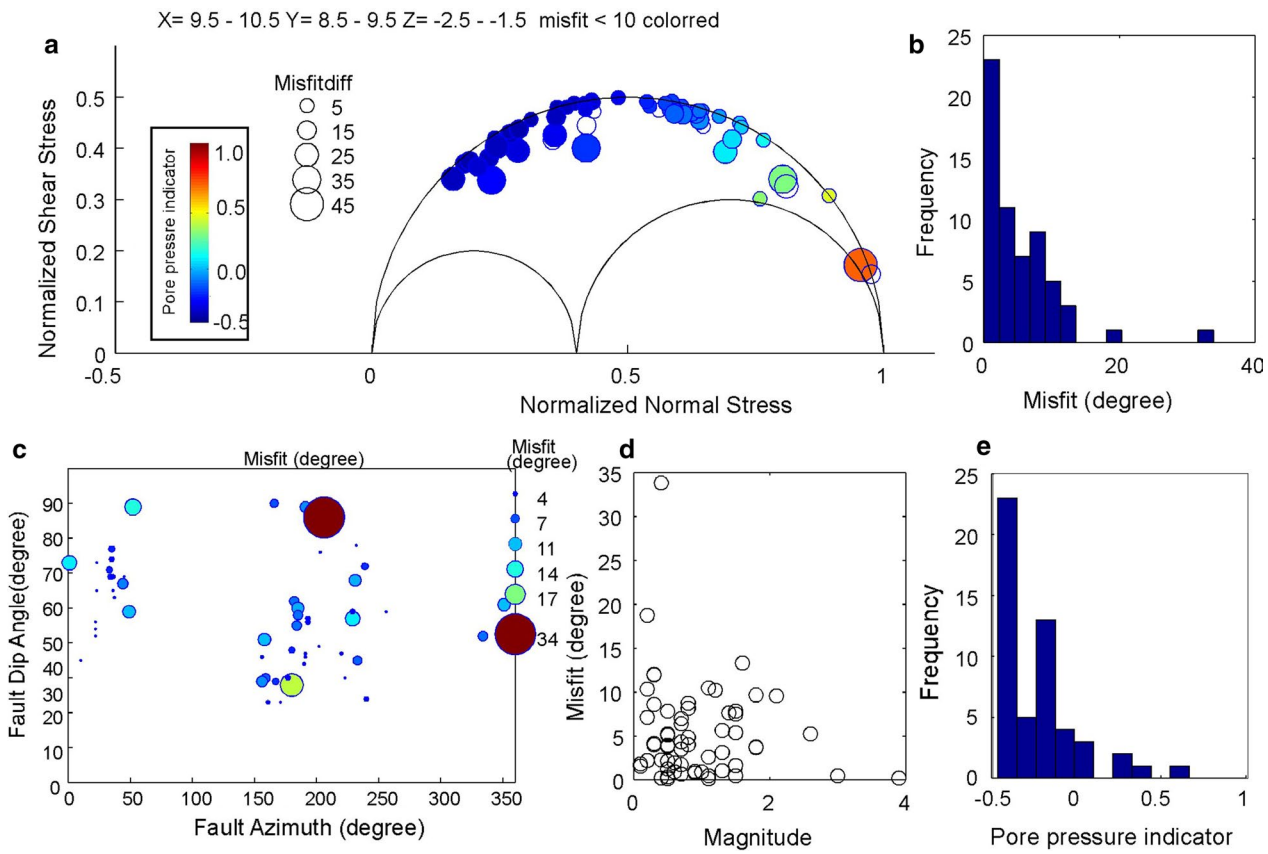

Fig. 12 **a** Plots of the normalized shear and normal stresses on a three-dimensional Mohr diagram for a grid point ($x = 9, y = 6, z = -2$). **b** Histogram of misfits. **c** Relationship between azimuths and dip angles of the fault planes. **d** Relationship between magnitude and misfit. **e** Histogram of the pore pressure indicator P_p. Other explanations are the same as for Fig. 10. The following figure is that for Fig. 10

plots are displayed for Kagan angles between the focal mechanisms of each event pair. As shown in the upper panel, focal mechanisms varied widely even for short focal distances in this plot. Furthermore, the same analysis was performed for the data for a grid point ($x = 9$, $y = 6$, $z = -3$) near the earthquake fault, and similar results were obtained, as shown in Fig. 14. Here, we have only displayed the results for two subregions; however, similar results were obtained for other subregions and for larger regions.

The orientations of *P*-axes varied widely even over very short distances. This finding strongly indicates that stress was not heterogeneous, but that strength was, because stress should hold for the condition of continuity and show some correlation with focal distance.

Fault strength

In this study, it was found that a major proportion of the data had misfits smaller than 10°. These results indicate that the observed focal mechanisms were well explained by uniform stress estimated for each grid point. Thus, it is thought that the variety of focal mechanisms shown in Figs. 9 and 11 are attributed to the strength of the faults. The variation was quantitatively measured based on the parameter P_p, and even P_p values larger than zero, namely larger than σ_3, were estimated, as shown in Figs. 10 and 12. Recently, high pore pressures have been estimated

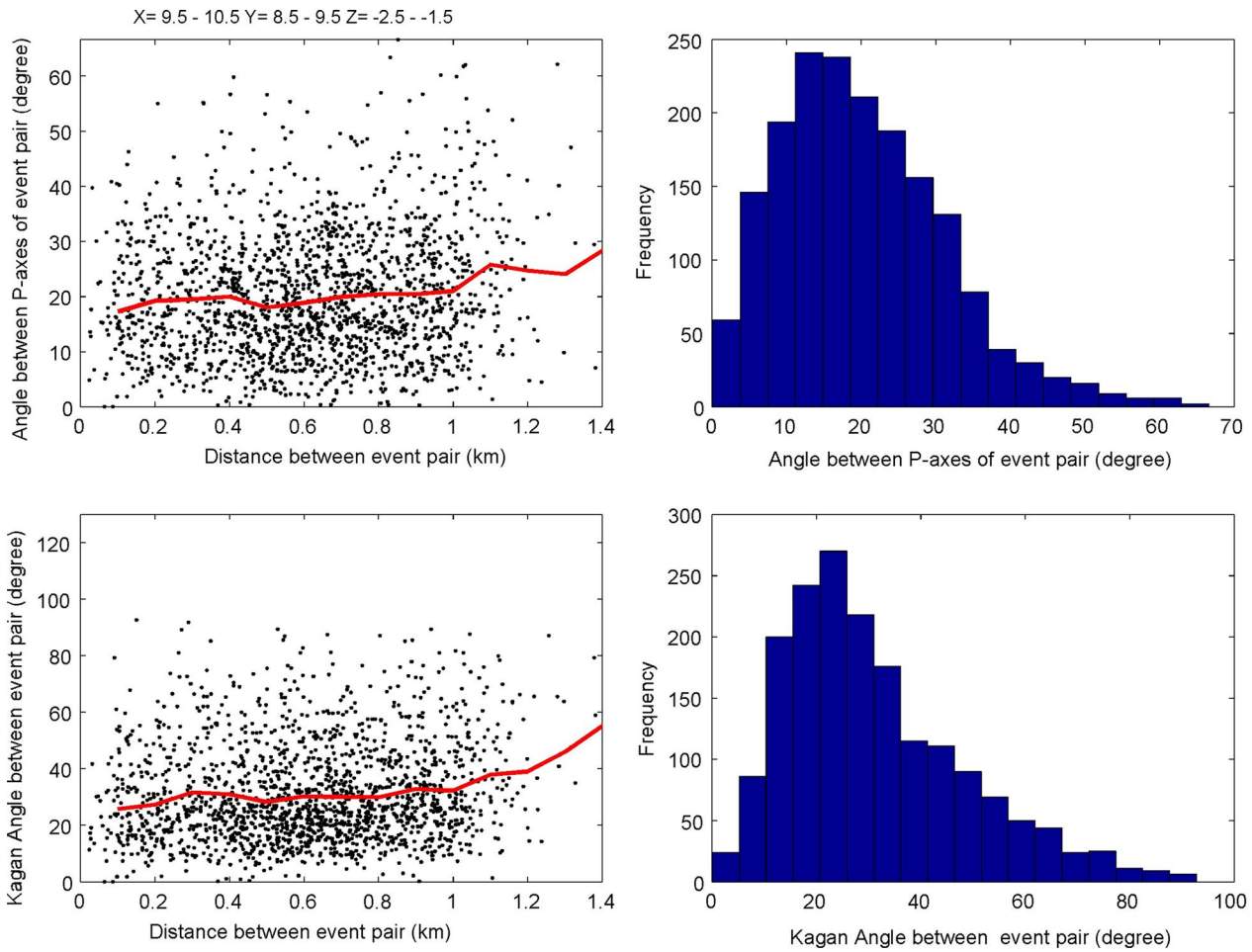

Fig. 13 (Upper) Relationship between focal distance and the difference in *P*-axis orientations (the angle between two *P*-axes) for each event pair in the cubic subregion for a grid point ($x = 10, y = 9, z = -2$), and the frequency distribution of angles between two *P*-axes of each event pair. (Lower) Similar plots for Kagan angles between focal mechanisms of each event pair

from analyses of focal mechanisms (e.g., Terakawa et al. 2010; Teradata et al. 2012). A portion of P_p values estimated in this study were too large to be regarded as pore pressure, because they exceeded the magnitude of the minimum compressional stress. These results suggest the possibility that there exists a mechanism by which fault strength is reduced without high pore pressure.

Conclusions

Using data from the high-density seismic observation networks installed in the western Nagano prefecture region, we precisely determined focal mechanisms and estimated the high-resolution stress field at a scale of 1 km. We found that nearly vertical σ_2 axes are concentrated around the mainshock fault, which is attributed

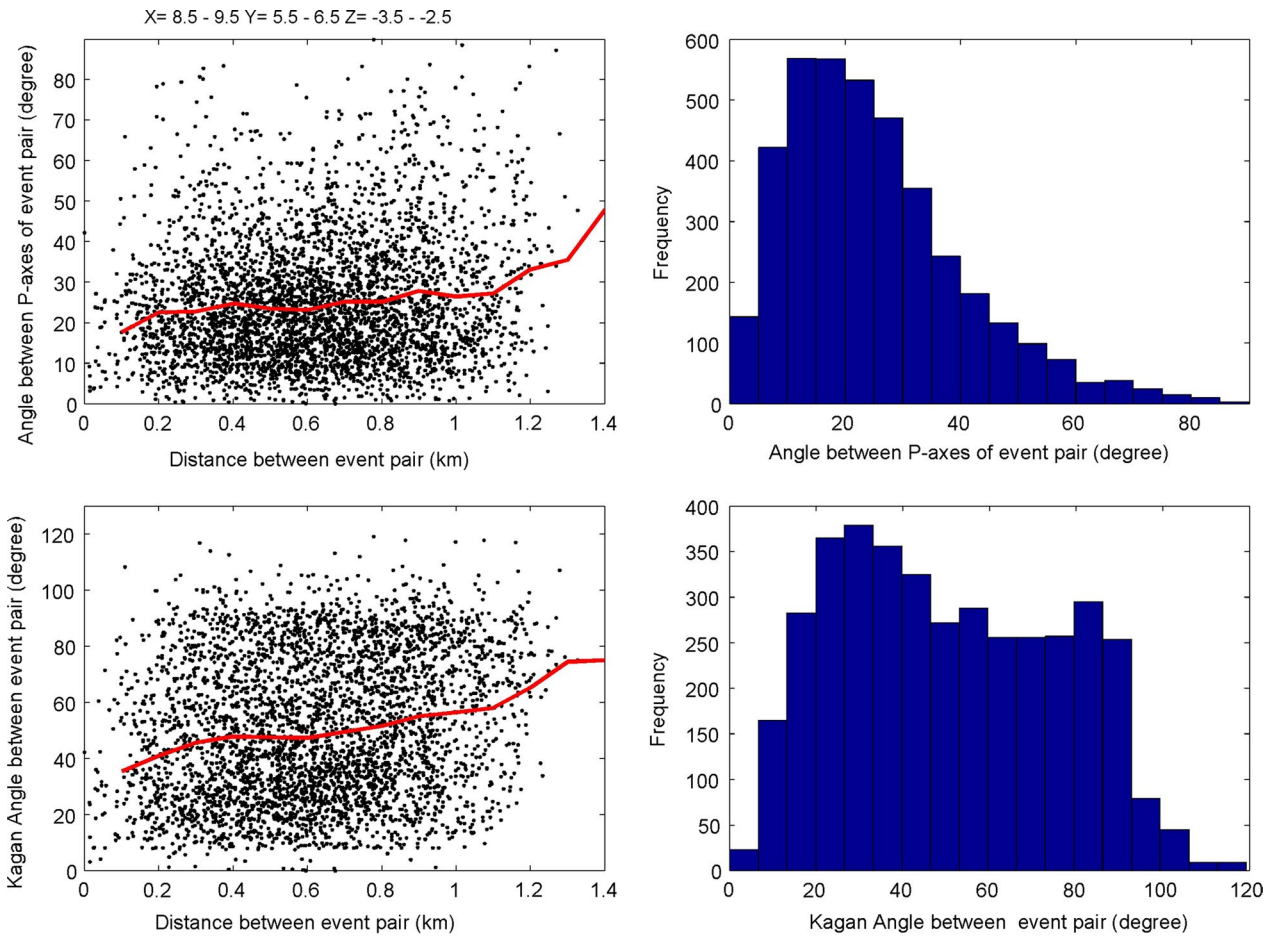

Fig. 14 (Upper) Relationship between focal distance and the difference in *P*-axis orientations (the angle between two *P*-axes) for each event pair at a grid point ($x = 9, y = 6, z = -3$), and the frequency distribution of angles between two *P*-axes of each event pair. (Lower) Similar plots for Kagan angles between focal mechanisms of each event pair

to aseismic slip in the downward extension of the mainshock fault, as pointed out by Yukutake et al. (2010). The root mean squares (RMSs) of differences between the observed and calculated slip directions (misfit) are smaller than the errors for focal mechanisms at grid points away from the mainshock fault. These findings clearly indicate that the estimated uniform stress well explains focal mechanisms in each subregion away from the mainshock fault. Although it appears at grid points near the mainshock fault that more than half of RMS misfits are larger than the errors in focal mechanisms attributed to the mainshock slip, close inspections of misfits for individual subregions revealed that many of the misfits are smaller than the error in focal mechanisms, and that stress can be regarded as uniform for a larger portion within each subregion. However, we found that focal mechanisms and *P*-axes vary widely and differ from each other over a short focal distance of 100 m. These results clearly show that stress can generally be regarded as uniform, but that strength is heterogeneous.

Authors' contributions

YI carried out data acquisition, processing and analysis. IY, TM, and YT carried out data acquisition. MS and SG contributed to data processing. KO and HK supervised the research. All authors read and approved the final manuscript.

Authors' information

YI, IY, MS, TM, and HK are members of the Manten seismic observation project. YT worked at the Kamitakara observatory near the Western Nagano prefecture region and joined in maintenances of the dense network. KO is the responsible person of the NIED joint project. HK is a gifted programmer and developed automated and manual phase picking programs.

Author details

[1] Research Center for Earthquake Prediction, Disaster Prevention Research Institute, Kyoto University, Uji, Japan. [2] Department of Earth and Planetary Sciences, Hokkaido University, Sapporo, Japan. [3] National Research Institute for Earth Science and Disaster Prevention, Tsukuba, Japan. [4] Home Seismometer, Fukushima, Japan.

Acknowledgements
We are grateful to the landowners and people in Ohtaki Village and Kiso Town in Nagano Prefecture for their great help in conducting seismic observations. We are also grateful to the staffs of the local and prefectural governments and for their assistance with our study. We used seismic data from the National Research Institute for Earth Science and Disaster Prevention (NIED), the Japan Meteorological Agency (JMA) and Nagoya University.

Competing interests
The authors declare that they have no competing interests.

Availability of data and materials
The data are basically utilized through cooperative studies.

Funding
This study was partly supported by the Ministry of Education, Culture, Sports, Science and Technology (MEXT) of Japan, under the Earthquake and Volcano Hazards Observation and Research Program, and KAKENHI Grant Number 26109006.

Publisher's Note

Received: 22 April 2017 Accepted: 11 October 2017
Published online: 20 October 2017

References

Andrews DJ (1980) A stochastic fault model: 1. Static case. J Geophys Res 85:3867–3877
Asaka Y, Iio Y, Shibutani T, Yukutake Y, Takai K, Horiuchi S (2005) Large-scale fault plane of the western Nagano Prefecture region estimated from precise hypocentral distribution. AGU 2005 Fall Meeting S41b-0987
Barton CA, Zoback MD (1994) Stress perturbations associated with active faults penetrated by boreholes: possible evidence for near-complete stress drop and a new technique for stress magnitude measurement. J Geophys Res 99:9373–9390
Ben-Zion Y, Sammis CG (2003) Characterization of fault zones. Pure appl Geophys 160:677–715
Byerlee J (1978) Friction of rock. Pure appl Geophys 116(4–5):615–626. doi:10.1007/BF00876528
Cheng X, Niu F, Silver PG, Horiuchi S, Takai K, Iio Y, Ito H (2007) Similar microearthquakes observed in western Nagano, Japan, and implications for rupture mechanics. J Geophys Res 112:B04306. doi:10.1029/2006JB004416
Doi I, Noda S, Iio Y, Horiuchi S, Sekiguchi S (2013) Relationship between hypocentral distributions and Vp/Vs ratio structures inferred from dense seismic array data: a case study of the 1984 western Nagano Prefecture earthquake, central Japan. Geophys J Int 195:1323–1336
Gephart JW, Forsyth DW (1984) An improved method for determining the regional stress tensor using earthquake focal mechanism data: application to the San Fernando earthquake sequence. J Geophys Res 89:9305–9320
Hardebeck JL (2010) Aftershocks are well aligned with the background stress field, contradicting the hypothesis of highly heterogeneous crustal stress. J Geophys Res 115:B12308. doi:10.1029/2010JB007586
Hardebeck JL (2015) Comment on "Models of stochastic, spatially varying stress in the crust compatible with focal-mechanism data, and how stress inversions can be biased toward the stress rate" by Deborah Elaine Smith and Thomas H. Heaton. Bull Seismol Soc Amer 105(1):447–451
Hardebeck JL, Hauksson E (2001) Crustal stress field in southern California and its implications for fault mechanics. J Geophys Res: Solid Earth 106 (B10):21859–21882
Hirata N, Matsu'ura M (1987) Maximum-likelihood estimation of hypocenter with origin time eliminated using nonlinear inversion technique. Phys Earth and Planet Inter 47:50–61
Hauksson E (1994) State of stress from focal mechanisms before and after the 1992 Landers earthquake sequence. Bull Seismol Soc Am 84:917–934
Iio Y (2009) Earthquake nucleation process: does the initiation of earthquake rupture know about its termination? In: Meyers RA (ed) Earthquakes, tsunamis, and volcanoes in encyclopedia of complexity and systems science. Springer, New York, pp 2538–2555
Iio Y (2011) Development of a seismic observation system in the next generation: to install ten thousands stations. Disaster Prev Res Inst Ann A 54A:17–24
Iio Y, Ohmi S, Ikeda R, Yamamoto E, Ito H, Sato H, Kuwahara Y, Ohminato T, Shibazaki B, Ando M (1999) Slow initial phase generated by microearthquakes occurring in the Western Nagano Prefecture, Japan: the source effect. Geophys Res Let 26:1969–1972
Imanishi K, Takeo M, Ellsworth WL, Ito H, Matsuzawa T, Kuwahara Y, Iio Y, Ohmi S (2004) Source parameters and rupture velocities of microearthquakes in Western Nagano, Japan, determined using stopping phases. Bull Seismol Soc Ame 94(5):1762–1780
Kagan YY (1991) 3-D rotation of double-couple earthquake sources. Geophys J Int 106:709–716
Kawanishi R, Iio Y, Yukutake Y, Shibutani T, Katao H (2009) Local stress concentration in the seismic belt along the Japan Sea coast inferred from precise focal mechanisms: implications for the stress accumulation process on intraplate earthquake faults. J Geophys Res 114:B01309. doi:10.1029/2008JB005765
Maeda N (1992) A method of determining focal mechanisms and quantifying the uncertainty of the determined focal mechanisms for microearthquakes. Bull Seismol Soc Am 82:2410–2429
Matsuzawa T, Takeo M, Ide S, Iio Y, Ito H, Imanishi K, Horiuchi S (2004) S-wave energy estimation of small-earthquakes in the western Nagano region, Japan. Geophys Res Lett 31(3):L03602. doi:10.1029/2003GL018445
Michael AJ (1984) Determination of stress from slip data: faults and folds. J Geophys Res 89(B13):11517–11526
Michael AJ (1987) Stress rotation during the Coalinga aftershock sequence. J Geophys Res 92:7963–7979
Michael AJ, Ellsworth WL, Oppenheimer DH (1990) Coseismic stress changes induced by the 1989 Loma Prieta, California earthquake. Geophys Res Lett 17(9):1441–1444
Rivera L, Kanamori H (2002) Spatial heterogeneity of tectonic stress and friction in the crust. Geophys Res Lett 29(6):1088. doi:10.1029/2001GL013803
Rydelek PA, Horiuchi S, Iio Y (2002) Spatial and temporal characteristics of low-magnitude seismicity from a dense array in western Nagano Prefecture, Japan. Earth Planets Space 54(2):81–89. doi:10.1186/BF03351709
Smith DE, Heaton TH (2011) Models of stochastic, spatially varying stress in the crust compatible with focal-mechanism data, and how stress inversions can be biased toward the stress rate. Bull Seismol Soc Am 101:1396–1421. doi:10.1785/0120100058
Teradata T, Miller SA, Deichmann N (2012) High fluid pressure and triggered earthquakes in the enhanced geothermal system in Basel, Switzerland. J Geophys Res. doi:10.1029/2011/JB008980
Terakawa T, Zoporowski A, Galvan B, Miller SA (2010) High-pressure fluid at hypocentral depths in the L'Aquila region inferred from earthquake focal mechanisms. Geology 38:995–998
Venkataraman A, Beroza GC, Ide S, Imanishi K, Ito H, Iio Y (2006) Measurements of spectral similarity for microearthquakes in western Nagano, Japan. J Geophys Res 111(B3):B03303. doi:10.1029/2005JB003834
Wilde M, Stock J (1997) Compression directions in southern California (from Santa Barbara to Los Angeles Basin) obtained from borehole breakouts. J Geophys Res 102(B3):4969–4983
Yoshida S, Koketsu K (1990) Simultaneous inversion of waveform and geodetic data for the rupture process of the 1984 Naganoken-Seibu, Japan, earthquake. Geophys J Int 103:355–362
Yoshida K, Hasegawa A, Okada T, Iinuma T (2014) Changes in the stress field after the 2008 M7.2 Iwate-Miyagi Nairiku earthquake in northeastern Japan. J Geophys Res 119:9016–9030
Yoshida K, Hasegawa A, Okada T (2015) Spatially heterogeneous stress field in the source area of the 2011 Mw6.6 Fukushima-Hamadori earthquake, NE Japan, probably caused by static stress change. Geophys J Int 201:1060–1069
Yukutake Y, Iio Y, Horiuchi S (2010) Detailed spatial changes in the stress field of the 1984 western Nagano earthquake region. J Geophys Res 115:B06305. doi:10.1029/2008JB006111